applied sciences

MDPI

Article

Production Optimization of Premium Food Can with Distortion Printing under Waving Requirement

Natthawat Chuchot [1] and Purit Thanakijkasem [2,*]

[1] Division of Materials Technology, School of Energy, Environment and Materials, King Mongkut's University of Technology Thonburi, Bangkok 10140, Thailand; natthawat.chuchot@gmail.com
[2] Division of Energy Management Technology, School of Energy, Environment and Materials, King Mongkut's University of Technology Thonburi, Bangkok 10140, Thailand
* Correspondence: purit.tha@kmutt.ac.th; Tel.: +66-2-470-8659

Featured Application: Optimization of premium food can production.

Abstract: This research aims to propose a novel approach for evaluating and minimizing scraps in an industrial production of premium food cans with distortion printing. Beyond conventional formability criteria, a waving requirement is introduced to ensure aesthetic quality of the printed graphics. The research focuses on real production conditions, specifically involving double-cold-reduced (DR) low-carbon steel sheets and chromium-coated tin-free steel with a thickness of 0.16 mm. The sheets are laminated on both sides with a plastic film prior to undergoing distortion printing on the exterior. Subsequently, a blank is subjected to a drawing-redrawing process to form a food can. To address challenges associated with characterizing these thin sheets, a material parameter identification method is proposed and demonstrated. The thickness profile and flange length are identified as key criteria for this identification process. Measurements of thickness distribution and flange length are obtained using digital image correlation (DIC) and microscopy techniques. Within the manufacturing system, uncertainties related to material properties and forming processes can result in scraps or defects. To analyze these processes, finite element analysis (FEA) is employed and validated through experiments. For the evaluation of scrap rates, uncertainty propagation is conducted using a metamodeling technique, specifically employing radial basis function (RBF) neural networks. The study concludes by offering process optimization recommendations aimed at reducing the scrap rate.

Keywords: waving; scrap rate; distortion printing; food can production; parameter identification

Citation: Chuchot, N.; Thanakijkasem, P. Production Optimization of Premium Food Can with Distortion Printing under Waving Requirement. *Appl. Sci.* **2024**, *14*, 7399. https://doi.org/10.3390/app14167399

Academic Editor: Ángel J. Gutiérrez Fernández

Received: 21 July 2024
Revised: 15 August 2024
Accepted: 17 August 2024
Published: 22 August 2024

1. Introduction

Metal packaging has gained popularity due to its environmental benefits, as it is 100% recyclable. Its ability to be sterilized with heat, cost effectiveness, strength, and short filling time also enhance its relevance. The most popular type of metal packaging is food cans, also known as sanitary food cans. The ratio of oxygen transmission rates (ORT) and water vapor transmission rates (WVTR) significantly impacts shelf life [1]. Metal cans provide a complete barrier against air and moisture, allowing canned food to be stored for at least two years [2]. Can packaging increasingly involves combining metal with other packaging materials such as laminated steel with plastic film. A new polyethylene terephthalate (PET)-laminated tin-free steel (TFS) sheet of low-carbon aluminum-killed steel for deep drawing processes in food cans has been developed and utilized in industry [3]. There is an increasing demand among customers for premium packaging solutions. Food can manufacturers have two primary labeling options: (1) paper labeling and (2) distortion printing, as illustrated step-by-step from a flat sheet to a finished product in Figure 1. Offset printing involves applying ink and varnish to flat sheets before the drawing and re-drawing (DRD) process.

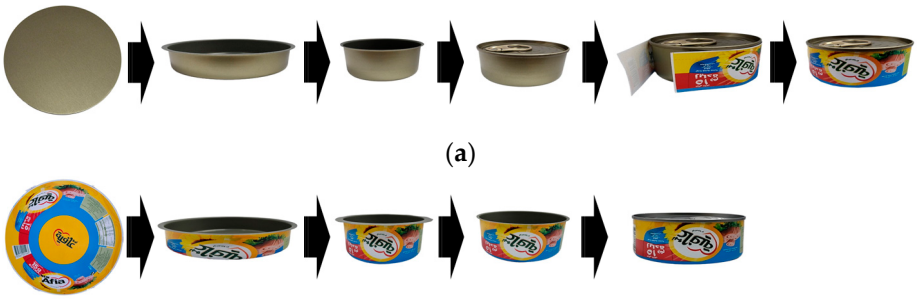

(**a**)

(**b**)

Figure 1. Food can labels: (**a**) paper labeling; (**b**) distortion printing.

Today, manufacturing business operators are striving to enhance product quality and accelerate the development of various technologies. Quality is one of the leading criteria in a business success. Total productive maintenance (TPM) is deployed inside the metal-forming industry to improve metal industry workstations, and the overall equipment effectiveness (OEE) is utilized in [4]. The deep drawing process is crucial to the metal food packaging industry, with a high production rate and excellent dimensional accuracy. Utilizing a very thin steel sheet, which possess high hardness and high yield strength, is a key aspect of this production.

Designing tooling and determining production parameters can be challenging due to the need for extensive trial and error to achieve optimal tooling shapes and production conditions. Advanced computer modeling to simulate metal-forming behavior is vital in reducing the time and cost associated with trial and error. Waving failure is a significant issue in distortion printing food cans, whereas it is not a concern in traditional cans. Figure 2 shows an accepted can and a rejected can due to the waving defect. The red circle in the figure shows the graphical distortion as a defect. For general practice in industry, a can with a waving height greater than 1.0 mm is rejected. A visual inspection in a real production line after several engineering improvements has revealed a scrap rate of 1.59%, significantly higher than the target of 0.25%. A high scrap rate indicates a low production and quality control efficiency, adversely affecting production output and manufacturing costs.

(**a**) (**b**)

Figure 2. Waving requirement in food can production: (**a**) accepted; (**b**) rejected.

FEA is an important tool for analyzing and designing the DRD process. Discrepancies between FEA and experimental results can arise from numerical errors in the FEA or changes in input variables. Numerous studies have utilized FEA to deterministically solve sheet metal-forming problems. For instance, the effects of tooling conditions on the deep drawing process of C.R.1 steel cylindrical cups with an initial thickness of 0.9 mm are studied using FEA and experimental methods in [5]. The forming optimization of ultra-low carbon steel with a thickness of 0.7 mm via inverse evolutionary search is presented in [6]. Optimization and tolerance prediction of mild steel with thicknesses of 0.725 and 0.775 mm are illustrated using a response surface model in [7]. For some issues with material models, such as 2090-T3 aluminum alloy with a thickness of 1.6 mm, a strong asymmetry between tensile and compressive behaviors is shown in [8]. Dual-phase steel (DP600) with a thick-

ness of 1.00 mm is experimentally investigated at a large strain in [9]. An application of isogeometric algorithms for one-step inverse steel forming with a thickness of 0.8 mm is presented in [10].

To improve quality, it is essential to account for uncertainty in the design process. Several studies have addressed uncertainties in sheet metal forming. A methodology for reliability calculations of structures to estimate the reliability of 0.81 mm sheet metal-forming operations using forming limit diagrams (FLD) to assess material breakage is presented in [11]. A metamodel of linear and quadratic interpolation response surfaces to evaluate the reliability of the sheet metal-forming process of an austenitic stainless steel named HyTens 800 with a thickness of 1 mm using the LS-DYNA solver and Monte Carlo simulation (MCS) is presented in [12]. Integration of MCS, the response surface method, and most probable point analysis to quantify probabilistic characteristics of shape and dimensional errors in forging and extrusion to minimize systematic errors is presented in [13]. A comparison between stochastic and interval methods for uncertainty quantification of the springback of a simple flanging of 1 mm steel sheet is presented in [14].

The uncertainty analysis of the deep drawing of aluminum alloy AA 5754-O with a thickness of 1 mm, using a quarter model of C3D8R, ABAQUS/Explicit solver, and surrogate model, is presented in [15]. A numerical tool to predict the uncertainties resulting in manufacturing products constituted by compliant lightweight parts in composite material joined by means of an adhesive is presented in [16]. A performance comparison of various parametric and non-parametric metamodeling techniques when applied to the U-Channel and the Square Cup forming processes is presented in [17]. A procedure to evaluate the robustness of defect and cost predictions in quality inspections of low-volume productions (e.g., a few tens per year of a hardness-testing machine), addressing how model uncertainties for defectiveness prediction can be assessed as well as their impact on selecting effective and affordable inspection strategies, is presented in [18]. A procedure combining response surface methodology (RSM) with FEA and MCS is applied to a real stamping process (LNE 380 steel transmission cross member) to optimize experimental problems with multiple responses, incorporating uncertainties in empirical function coefficients, as presented in [19]. A strip drawing test utilizing flat dies is conducted on cold-rolled low-carbon DC06 steel sheets to model friction behavior within the drawpiece flange region, and a radial basis function (RBF) neural network is employed to investigate the influence of individual friction parameters on the coefficient of friction (COF) in [20]. An application of temporal signal processing and artificial intelligence (AI) to monitor and optimize can rolling processes within the oil and gas industry is tested, and the methodology is able to identify patterns and anomalies in the production data, as presented in [21]. A methodology for optimizing the deep drawing process of a T-shaped component fabricated from 0.75 mm DC05 steel is presented in [22]. Their approach, aligned with Industry 4.0 principles, involves utilizing the blank holder force as a dynamic process variable, adjusted in real-time based on specific draw-in points during the punch stroke. The goal is to enhance component quality. However, it is important to acknowledge that the implementation of a variable blank holder force during the punch stroke may not be feasible in many industrial production environments.

Most of the literature addresses steel with a thickness of approximately 1 mm, which is not as thin as the sheet used in this study and often overlooks uncertainty in the process analysis and/or design. This work focuses on a relatively new material with a smaller thickness and considers uncertainty in a real production. Additionally, this paper explores strategies to reduce the scrap rate relevant to the industry. There are few studies in the literature focusing on new industrial food can production with distortion printing to evaluate and improve the scrap rate under waving criteria and uncertainty. This paper subsequentially presents waving defects in food can forming, material testing, simulation, material parameter identification, scrap rate assessment, and production optimization, fostering a more robust connection with practical manufacturing processes.

2. Waving Defect in Food Can Forming

Manufacturers of food cans with distortion printing have serious concern about defects related to the waving requirement. This section outlines the issues associated with distortion printing in food cans, the can-forming process, the analysis of can forming, and the definition of waving failure.

2.1. Distortion Printing in Food Can

Currently, the premium can production industry, which relies on distortion printing, has elevated its requirements beyond mere engineering functions. The DRD process is essential in the manufacturing of food cans. The industry defines the product code as ABCxDEF. For example, 307 × 113 is a can with a diameter of 307 (i.e., 3 + 07/16 inch) and a height of 113 (i.e., 1 + 13/16 inch). Currently, the factory in this study produces the following DRD food cans: 307 × 113 (40%), 211 × 109 (20%), 300 × 103 (16%), 300 × 200 (14%), and others (10%). This study focuses on the 307 × 113 DRD as the case study.

Achieving a successful food can with distortion printing requires both art and science of forming. For the 307 × 113 DRD, an industrial guideline is shown in Figure 3 and includes the following recommendations: To minimize the scrap rate, text should not be placed within 6 mm from the bottom edge or within 8 mm from the top or seamed edge. Additionally, graphic designs featuring text or straight lines in these areas are susceptible to a distorted display.

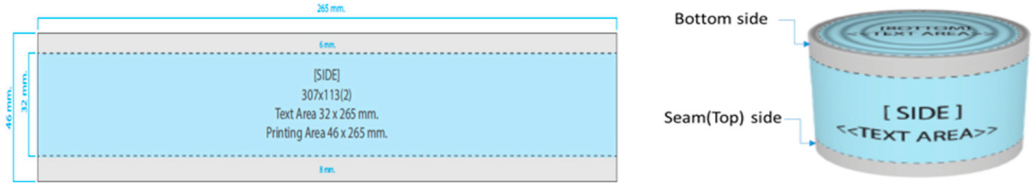

Figure 3. Guideline for design of distortion printing.

Distortion printing can be analyzed by printing a grid pattern on a flat sheet and then forming into the cylindrical shape of food cans. Grid technology is applied in the food can-forming process to produce new designs and prints. There are four stages in distortion printing: (1) A grid is printed on a flat sheet, and then, a can is formed; (2) the distorted grid is carefully analyzed by measuring the extent of distortion in each square to create a new distorted grid; (3) the new distorted grid is re-printed and then formed again (if it is a bad one, the process is repeated); and (4) once an accepted grid pattern is achieved, the new results are used to create the distorted artwork required by the customer's design. Notably, the uncertainty is not taken into account here. Figure 4 shows the design process on a sheet (36 cans per sheet). Grid adjustment can be performed using two methods: rotation and compensation. Rotation involves adjusting the grid so that the distorted area is free of graphics. Compensation involves pushing or pulling from the original grid. These grid adjustment methods are employed to mitigate waving problems. Figure 4d illustrates the method of correcting the printed image by rotating it from its original orientation. If the method illustrated in Figure 4d is tested and the image quality does not meet the specified standard, the compensation is implemented. Figure 4e demonstrates a method for correcting a printed image by continuously stretching or shrinking it. The image is locally stretched or contracted to compensate for the distorted image in the area requiring correction. In a preliminary trial prior to grid adjustment, the scrap rate is observed to be 8.33%, i.e., 150 scrap pieces from a test run of 1800 pieces. In a real production after the grid adjustment, the scrap rate decreases to 1.59%, i.e., 5649 scrap pieces from 356,229 pieces.

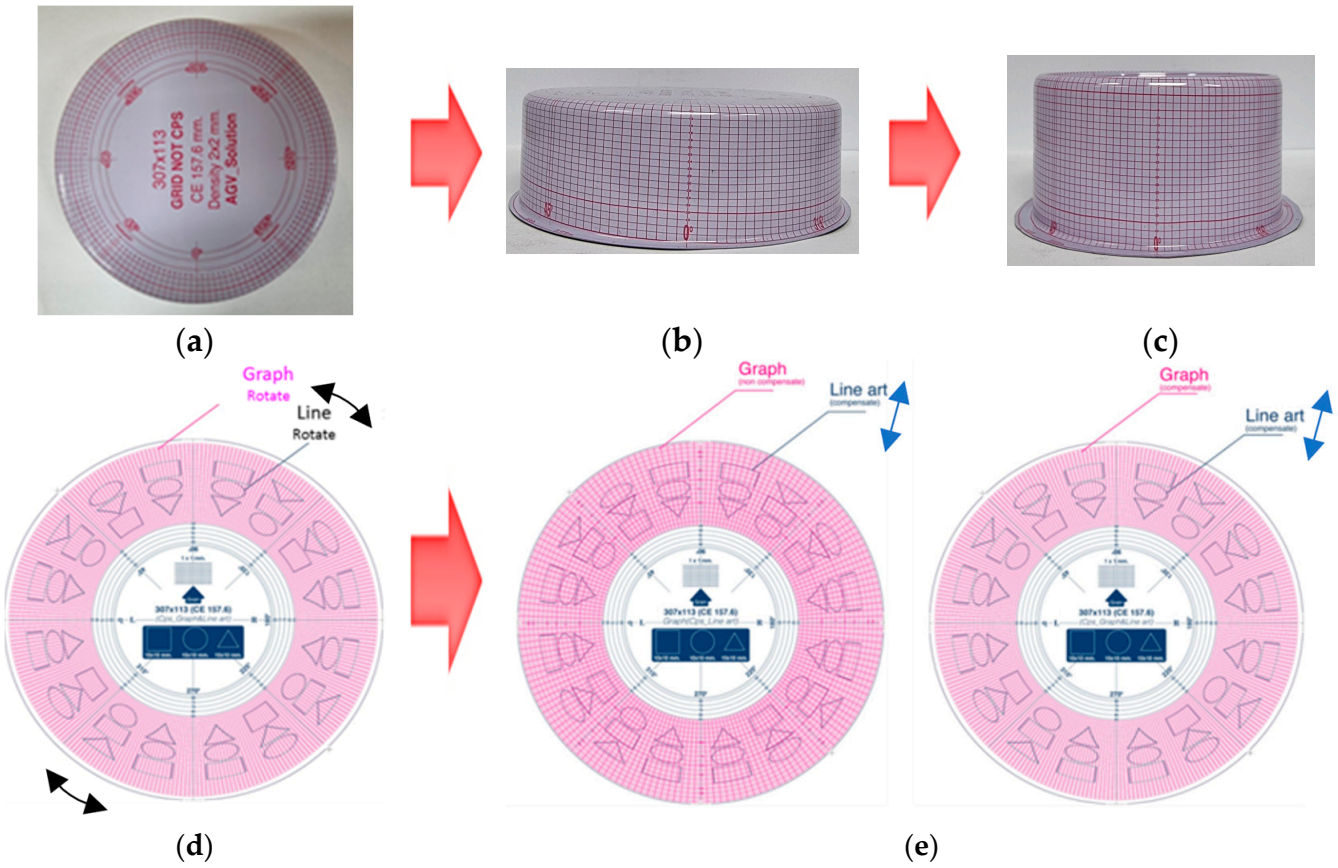

Figure 4. Design process of distortion printing: (**a**) flat sheet; (**b**) drawing; (**c**) redrawing; (**d**) layout of grid adjustment by rotation; (**e**) layout of grid adjustment by compensation.

2.2. Can-Forming Process

In the metal packaging industry, deep drawing is presumably carried out using rigid tools, which consist of a punch, a die, and a blank holder. The can-forming process begins with blanking a flat sheet. After the blank is inserted, the blank holder closes, clamping the sheet between the die and the blank holder. This action regulates the flow of the sheet during the drawing process, effectively preventing the formation of wrinkles beneath the blank holder. The punch then stretches the sheet over the die radius, shaping it within the die, while the required punch force progressively increases. The cup then undergoes re-drawing, and the final step is to trim the excess. The DRD process for the 307 × 113 DRD and the relevant tooling are shown in Figure 5. The initial blank diameter is 157.60 mm, while the outer diameters of the drawing and re-drawing are 114.10 mm and 83.75 mm, respectively. The tooling material used is JIS SKD11.

Lubricant plays an important role in the DRD process. In this production, a lubricant made from white mineral oil is applied to both sides of PET-laminated TFS sheets via rollers before forming. To simulate the DRD process, the coefficient of friction (COF) is required. COF of the TFS sheet is measured using a slip tester and a force gauge (Digicon, model FG-620SD), as illustrated in Figure 6. The tester complies with multiple national and international standards, including ASTM D1894, the standard test method for the COF of plastic film and sheeting. The measured COF of the TFS sheet after lubricant application is 0.03.

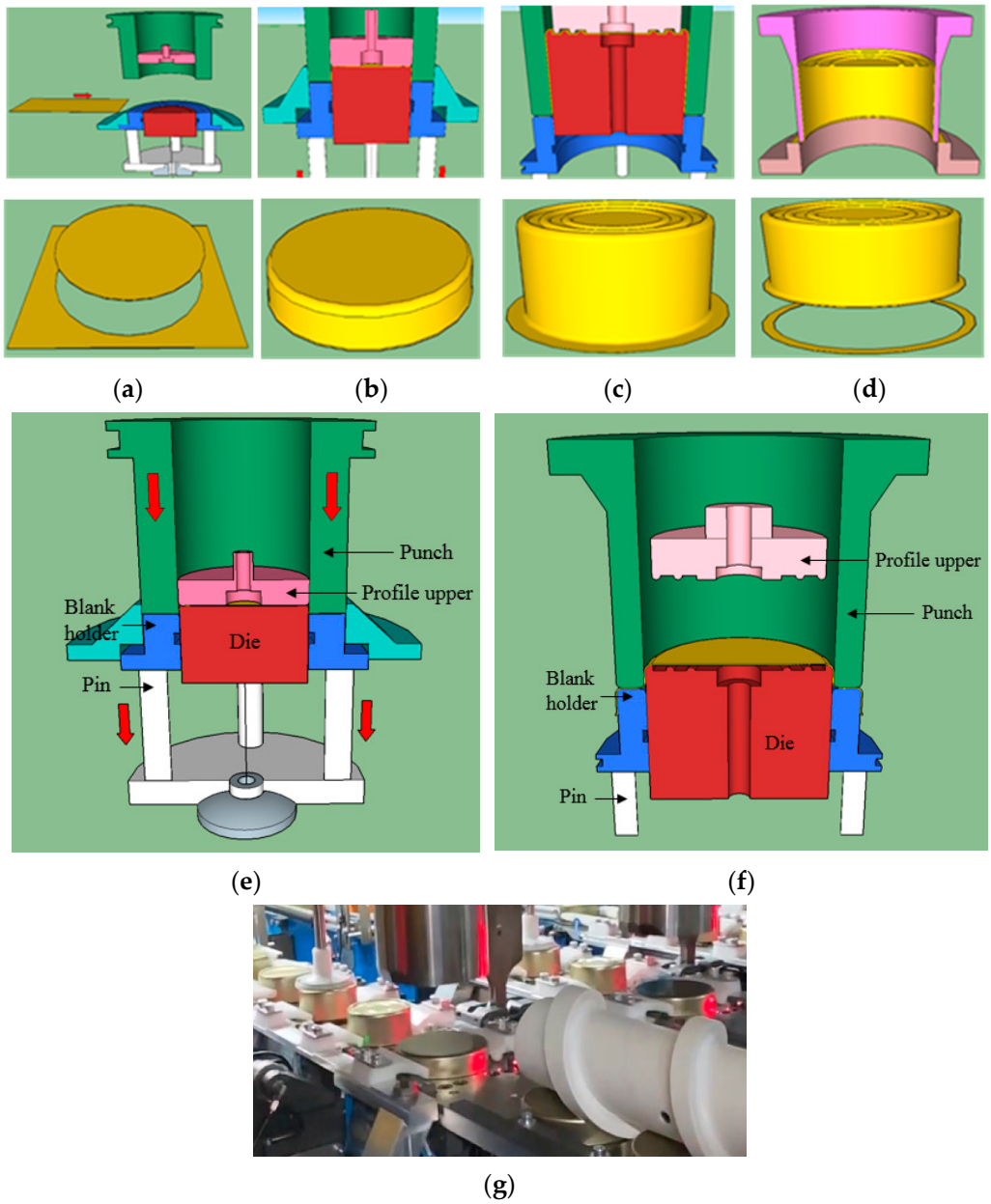

Figure 5. DRD process: (**a**) blanking; (**b**) drawing; (**c**) redrawing; (**d**) trimming; (**e**) drawing tooling; (**f**) redrawing tooling; (**g**) real production setup.

Figure 6. Friction tester: (**a**) setup; (**b**) force gauge; (**c**) weight 2.157 kg.

2.3. Analysis of Can Forming

One of the most significant industrial advantages of the deep drawing process is its high production rates. The success of FEA in the design and optimization of metal forming strongly depends on its ability to accurately describe the material's mechanical behavior. An FEA model needs the following: raw material properties, forming process parameters (e.g., formability, earing and waving evaluation, lubrication or surface properties, blank holder force, and tooling conditions), and the desired shape of the product.

In this study, three-dimensional FEA is utilized. The geometry of the drawing and redrawing processes is shown to be axisymmetric. The geometry of the FEA model is based on the tool set drawings acquired from the actual process. The can-forming process is simulated using a nonlinear explicit finite element method, with the LS-DYNA solver adopted for this work. The DRD process is shown in Figure 7.

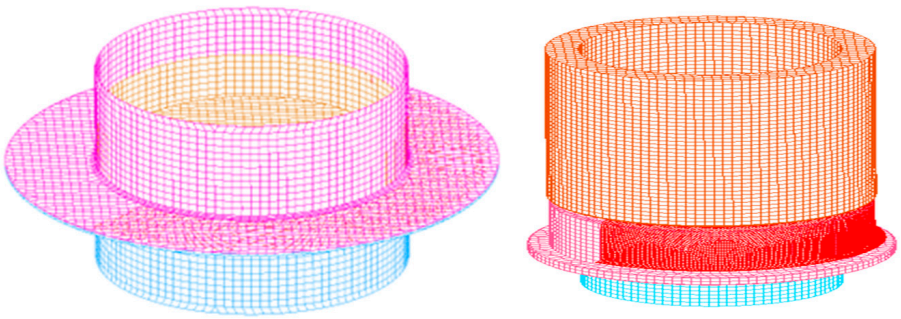

(**a**) (**b**)

Figure 7. DRD simulation via FEA: (**a**) drawing; (**b**) redrawing.

Shell elements are utilized to model both the tooling surface and the blank. Specifically, a shell element type utilizing the Belytschko–Tsay formulation, with seven integration points across the thickness and a shear correction factor of 0.833, is adopted. The tooling is represented as a rigid body, while the blank is modeled as deformable. The tooling speed is set at approximately 1000 mm/s, and Coulomb's friction model is applied. Adaptive meshing is not activated. For illustration, the formed part is modeled as a half model. For materials exhibiting a high degree of anisotropy, it may be necessary to employ a full 360-degree model. Alternatively, model verification should be conducted prior to adopting any model simplification. The material model applied is Barlat'89, with an exponent of 6.0 in the yield function. The material properties include a Young's modulus of 207 GPa, a tangent modulus of 100 MPa, a Poisson's ratio of 0.28, and a mass density of 7.83 g/mm^3. The PET-laminated TFS sheet is found to exhibit anisotropy based on tensile tests in Section 3.

Before using the FEA model developed in this section to further study the process, it needs validation to ensure the accuracy of the simulation results. This validation involved running the FEA model based on the actual process parameters used in the current production line.

2.4. Waving Failure Definition

The definition of waving is illustrated in Figure 8. Common waving locations in distortion printing are found on the sidewall of the food cans near the flange after redrawing. Waving can lead to customer complaints and claims. Despite implementing a modified design layout and corrective actions to address these waving issues, the problem persists.

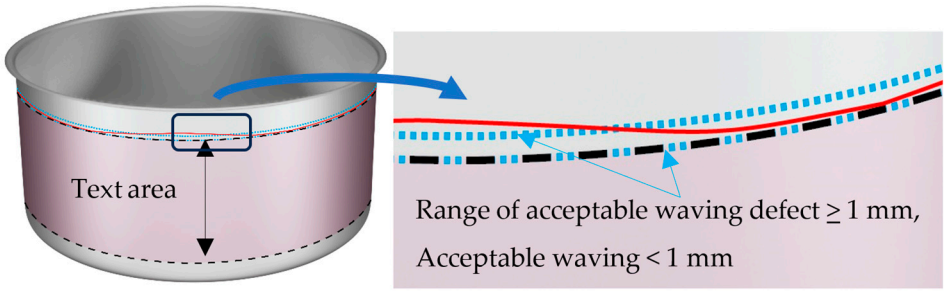

Figure 8. Definition of waving.

This study also aims to define the waving value using FEA. The center of the half-model blank is identified, with an initial radius of 78.8 mm. To define the waving value from material deformation, a group of nodes with a radius of 72.74 mm (92.3% of the initial radius) is selected, as shown in Figure 9. To accurately capture the waving value, an evaluation of the number of nodes (3, 5, 9, and 17) needed for the calculation is conducted. The distance range between 3, 5, and 9 nodes is approximately the same at 0.09, while that of 17 nodes is larger at 0.21. In this study, the group of 17 nodes is deemed suitable for defining the waving value (Z and ΔZ), as shown in Figure 10. An automated meshing approach is currently implemented. Nevertheless, to optimize the data acquisition for future waving evaluation, a manual meshing strategy is recommended to ensure uniformly distributed nodes.

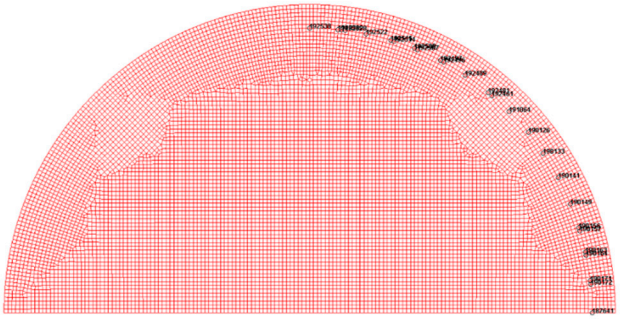

Figure 9. Selected nodes used to define waving value.

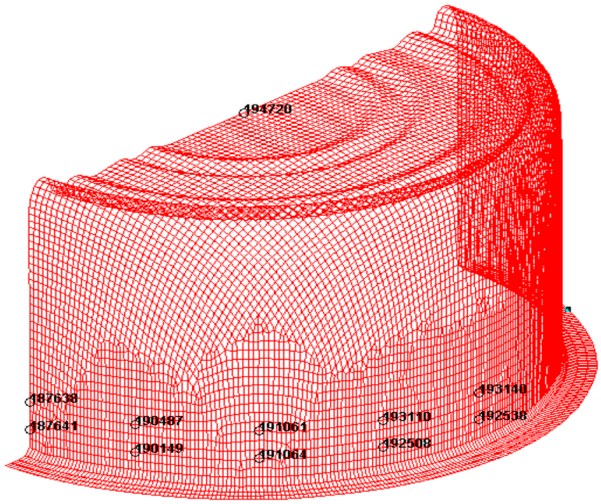

Figure 10. Nodes used to define the waving value (Z_1, Z_2, and ΔZ).

All selected nodes have a similar radial distance from the origin. At the end of the forming process, the Z-coordinates (vertical axis) of all selected nodes are retrieved

for further calculation. The waving value (ΔZ) is defined as the difference between the maximum and minimum Z values from all nodes. To avoid overlapping, only five points are shown in Figure 10. Z_1 represents the lower level, while Z_2 represents the upper level. ΔZ_1 from Z_1 is always greater than ΔZ_2 from Z_2. For example, at COF of 0.03 and BHF of 24,000 N, ΔZ_1 and ΔZ_2 are 0.92 and 0.75 mm, respectively. Consequently, only ΔZ from Z_1 is used for the waving evaluation.

3. Material Parameter Identification

This section focuses on material parameter identification, a crucial aspect of simulation. Steel for can making is supplied either as tin plate, which has a very thin layer of tin electrodeposited onto both sides, or as TFS, which contains no tin. The material used in this study is a TFS sheet (SPTFS in JIS G 3315: chromium-coated TFS). TFS is electrolytic chromium-plated steel consisting of a thin layer of chromium and a layer of chromium oxide deposited on a cold-rolled sheet steel base (black plate), giving it a beautiful, lustrous metallic finish on both sides. TFS is superior to tinplate for lacquer and plastic film applications, as it does not peel off, whereas tinplate is more prone to lacquer and plastic film peeling. This section includes an investigation of material properties via tensile tests, parameter identification via thickness distribution, and parameter identification via flange length.

3.1. Material Tests

The material used is a TFS sheet known as SPTFS MR DR-8 (JIS G 3315). This material offers superior performance in terms of resource conservation, energy efficiency, and environmental protection. The doubly reduced (DR) temper is produced to achieve extremely high-yield strength in chromium-coated TFS, as indicated by the Rockwell superficial hardness values (HR3TSm). Using the DR method, the base metal's thickness is reduced a second time on a temper mill after annealing, increasing material strength while decreasing elongation. This TFS sheet has a thickness of 0.16 mm and a hardness of DR-8. It is laminated on both sides with PET film, with a thickness of 13 microns on the outside and 20 microns on the inside.

In this application, there are two types of low-carbon steels: (1) aluminum-killed steel (Al-killed), which is deoxidized with aluminum during production to remove carbon monoxide, resulting in lower oxygen content and improved surface finish, and (2) super ultra-low-carbon (SULC) steel. The cost of SULC is approximately 2% higher than Al-killed steel. The main difference between these steels, based on the chemical composition of tin mill black plate (TMBP), is the carbon content. Al-killed steel has a higher carbon content (max 1600 ppm), while SULC steel has a lower carbon content (max 60 ppm). Other elements are largely the same, with Si = 400, P = 200, S = 500, and Mn = 6000 (max).

The mechanical properties are not uniform in all directions (anisotropy). Consequently, distortion printing results in waving, leading to a relatively high scrap rate in production. Tensile tests of those materials are conducted in three directions (RD (0°), DD (45°), and TD (90°)) at a speed of 5 mm/min using a Shimadzu Model Autograph AG-X plus 50 kN (Lab3) at 25 °C and 51% RH. The test results are averaged from five samples per direction. Both Al-killed and SULC steels have similar yield points and tensile strengths, as shown in Table 1. SULC offers better earing than Al-killed, as illustrated in Figure 11. Therefore, Al-killed steel is suitable for lacquering, while SULC is more suitable for distortion printing.

Further investigation of SULC is necessary within the context of distortion printing. The elongation observed in the test results presented in Table 1 is notably low, at less than 2%. Additionally, some of the test outcomes deviate from standard expectations, including unusually low R-values. According to ASTM E517, the appropriate strain level for determining the R-value is typically around 20%. To address this discrepancy, additional tests are conducted in collaboration with two laboratories. The averaged results from all three laboratories, across three directions, are presented in Table 2.

Table 1. Mechanical properties of Al-killed steel and SULC steel (from Lab 3).

Description	Al-killed Steel (Lacquering)			SULC Steel (Distortion Printing)		
	RD	**DD**	**TD**	**RD**	**DD**	**TD**
1. Yield point (MPa)	626	642	672	613	626	662
2. Tensile strength (MPa)	626	654	698	614	640	677
3. *R*-value	0.09	0.15	0.08	0.10	0.13	0.15
4. Elongation (%)	1.0	2.0	2.2	1.9	1.8	1.9

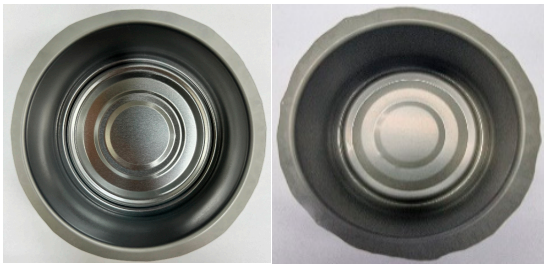

Better earing (**a**) Fair earing (**b**)

Figure 11. Earing and flange length from different materials: (**a**) SULC; (**b**) Al-killed.

Table 2. Mechanical properties of SULC obtained from 3 laboratories.

Description	Averaged Results								
	Lab 1			**Lab 2**			**Lab 3**		
	RD	**DD**	**TD**	**RD**	**DD**	**TD**	**RD**	**DD**	**TD**
1. Yield point (MPa)	448	423	427	500	519	539	613	626	662
2. Tensile strength (MPa)	468	440	434	517	534	567	614	640	677
3. *R*-value	0.15	0.10	0.17	0.40	0.54	0.60	0.10	0.13	0.15
4. Elongation (%)	n/a	n/a	n/a	n/a	n/a	n/a	1.9	1.8	1.9

The yield point and tensile strength values obtained from the three laboratories (Lab 1: ASTM E8, Lab 2: DIN 50114, and Lab 3: JIS No. 5) exhibit a significant discrepancy. The yield point determined by Lab 3 is selected for subsequent analysis due to its alignment with the industrial specification indicated in the datasheet. It is hypothesized that the thinness of the steel sheet may have contributed to these variations, as most testing apparatus are designed for materials with a thickness of approximately 1 mm. The quality of the cut edge may also contribute to the observed discrepancies, as the samples are produced using a punch press, which can induce minor edge deformations. Employing a more precise cutting method could potentially mitigate this issue.

Figure 12 displays the samples subjected to tensile tests in three directions from the three laboratories. The breakage exhibits minimal elongation, and necking is negligible, raising concerns about the accuracy of these tests, particularly *R*-value at 5% strain. The subsequent sections address the material parameter identification method proposed in this study. The normal anisotropy ratio ($\overline{R}$) is an averaged one from $(R00 + R90 + 2R45)/4$, while the planar anisotropy parameter (ΔR) is defined as $(R00 + R90 - 2R45)/2$, where $R00$, $R45$ and $R90$ are *R*-value at 0°, 45°, and 90°, respectively.

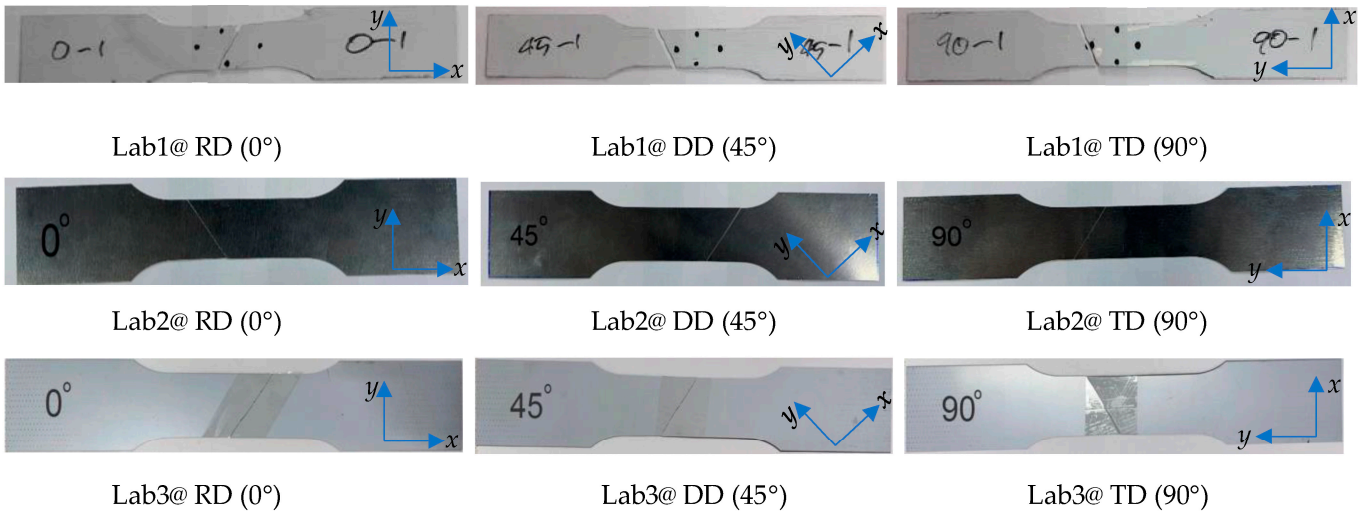

Figure 12. Samples after tensile tests for three directions from three labs.

3.2. Parameter Identification via Thickness Distribution

This section demonstrates the use of the inverse analysis to identify the material parameter, specifically the normal anisotropy ratio ($\overline{R}$). The thickness distribution, as shown in Figure 13, serves as the primary criterion. At each angle relative to the rolling direction, the thickness is measured at nine specified locations. While the initial sheet thickness is assumed to be constant, variations occur in certain areas due to the forming process.

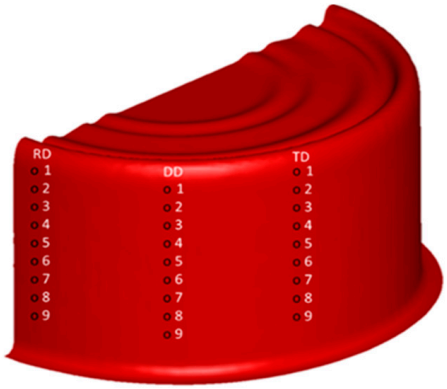

Figure 13. Thickness measurement locations on the sidewall.

The thickness distribution is examined through cross-sectional analysis. Specimens are prepared by molding them with resin and sectioning them in three directions (RD, DD, and TD). The molded specimens are ground and polished to reveal the thickness profiles, as shown in Figure 14. A digital microscope (Olympus, Model DSX500-MSU, resolution 0.01 µm) with a maximum magnification of 250×, along with image analysis software, is used to measure the thickness values at nine different locations per direction. For each location, three measurements are taken, and the average value is used to represent the thickness at that location.

Digital image correlation (DIC) is the second technique used to obtain thickness distribution. DIC evaluates the surface strain levels of sheet metal parts after forming. Prior to forming, laminated TFS blanks undergo grid marking using offset printing with a dot pattern (dot diameter of 1.5 mm and spacing of 2.0 mm), as shown in Figure 15.

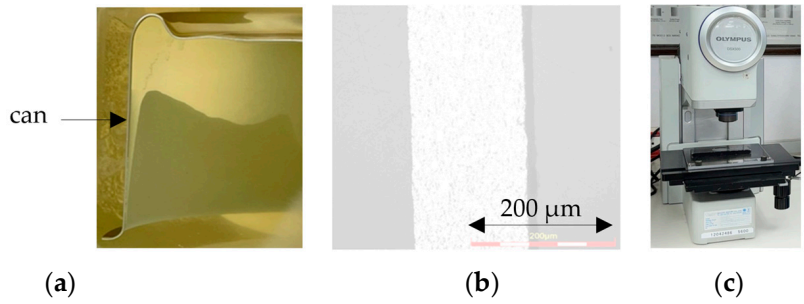

Figure 14. Thickness measurement: (**a**) molded specimens; (**b**) 250× image; (**c**) digital microscope.

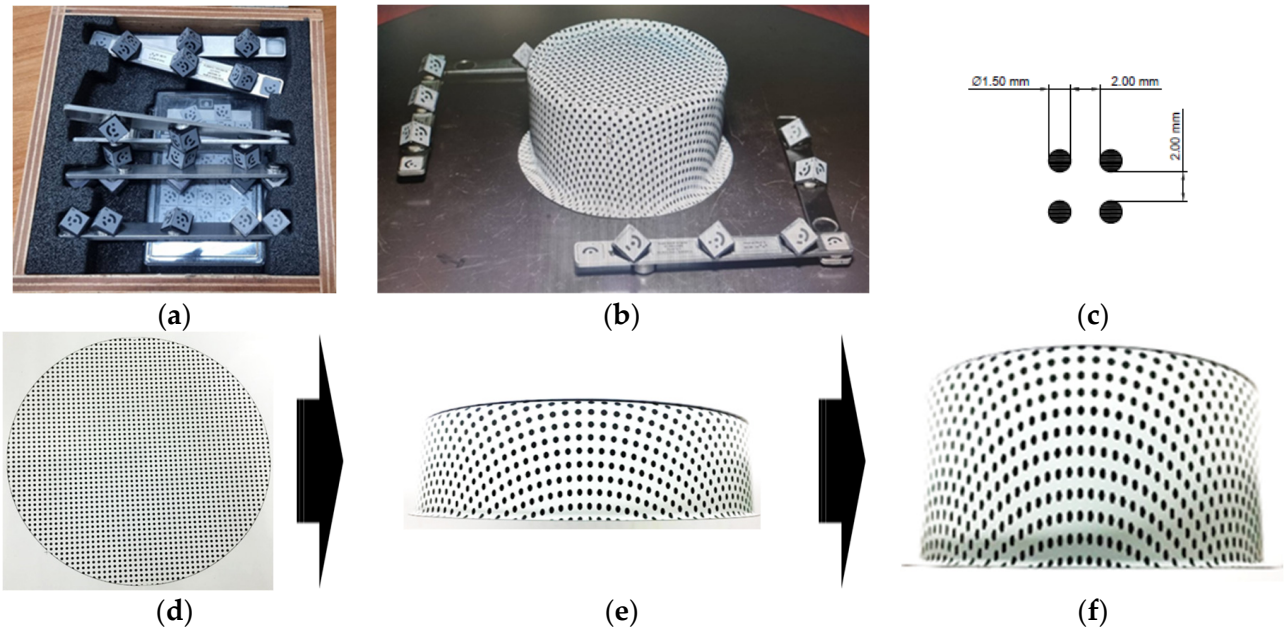

Figure 15. DIC measurement: (**a**) setup; (**b**) grid configuration; (**c**) flat sheet; (**d**) drawing; (**e**) redrawing.

After forming, the laminated TFS sheet is recorded from various viewing angles using the handheld ARGUS system, enabling the measurement of principal strains. The results provide strain distributions on the parts, including major and minor strains. ARAMIS sensors measure statically loaded specimens and parts using a contact-free, material-independent method based on the principle of DIC. Thickness is determined by the major and minor strains, assuming the constant volume deformation at RD, DD, and TD at nine different locations per direction. The thickness is calculated using the relationship $t = t_0 \cdot \exp(\varepsilon_t)$, where t is thickness, t_0 is base steel thickness of 0.16 mm, major strain is ε_1, and minor strain is ε_2 ($\varepsilon_t = -(\varepsilon_1 + \varepsilon_2)$), as shown in Figure 16.

The thickness distributions at nine locations on the can wall, obtained from ten samples using both microscopy and DIC, are compared and presented in Figure 17. The results from these two methods exhibit negligible differences and align with the trends reported in [23].

The thickness measurements at the nine locations are further analyzed using the sum of squared error (SSE), also known as the residual sum of squares, which represents the difference between the experimental values and FEA values. A lower SSE indicates a better agreement with the experimental data.

Figure 18 shows SSE thickness in relation to $\overline{R}$ (independent variables ranging from 0.3 to 0.9). It identifies an optimal $\overline{R}$ value at 0.5 in FEA for a die radius of 1.5 mm and COF of 0.03 as the process parameters.

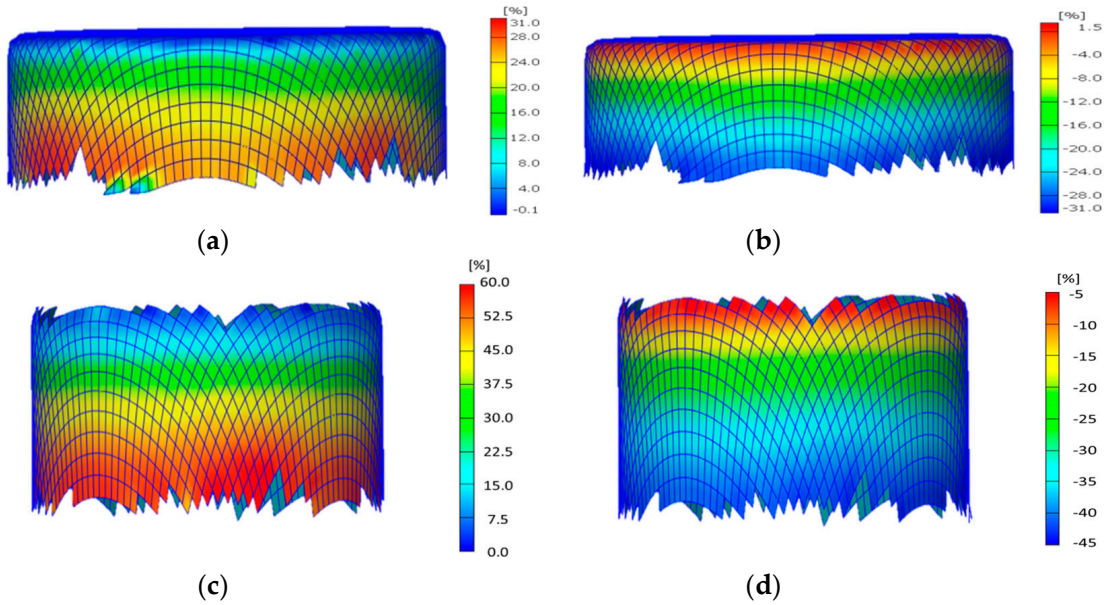

Figure 16. Strain distribution from DIC: (**a**) major strain after drawing; (**b**) minor strain after drawing; (**c**) major strain after redrawing; (**d**) minor strain after redrawing.

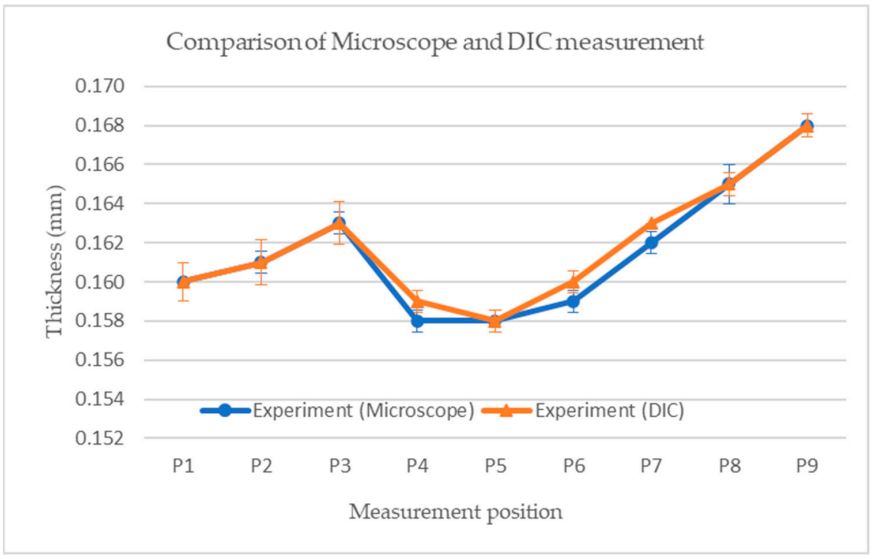

Figure 17. Comparison of microscope and DIC measurement.

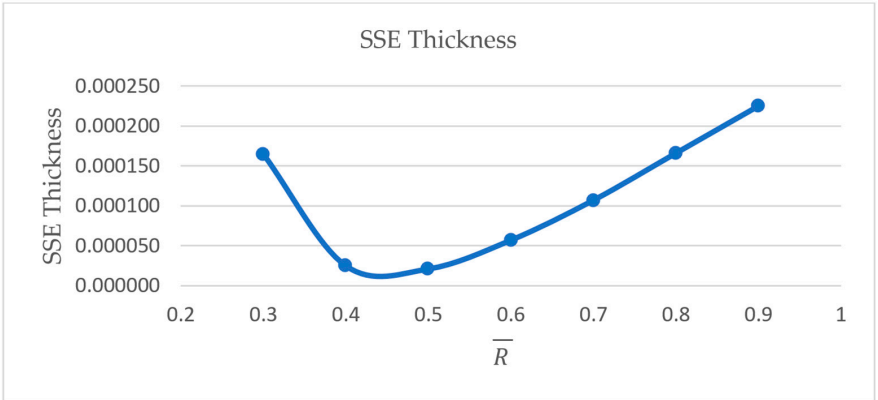

Figure 18. SSE average thickness as a function of $\overline{R}$.

Following the determination of $\overline{R}$, a comparison of the average thickness distribution on the can wall between experimental results (averaged from microscope and DIC) and FEA (with $\overline{R}$ of 0.5, COF of 0.03, and BHF of 16,000 N) is shown in Figure 19. The findings indicate that FEA can accurately predict the average thickness distribution, showing a good agreement with the experimental data.

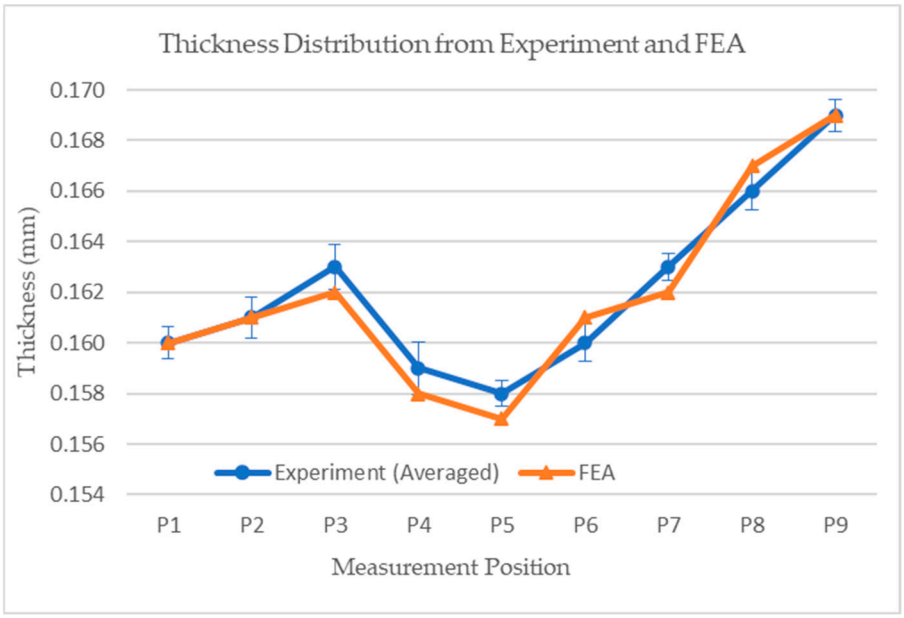

Figure 19. Comparison of averaged thickness distribution from experiment and FEA.

3.3. Parameter Identification via Flange Length

To identify R, the flange length of the can in a different direction is used. All cans are marked to indicate RD. The flange length at five locations after re-drawing from the experiment is measured using a digital microscope (Keyence, Model VHX-7000) with a maximum magnification of 30x. These five locations for SULC and Al-killed are shown in Figure 20 (labeled as follows: 1 = RD, 2 = 22.5°, 3 = DD, 4 = 67.5°, and 5 = TD).

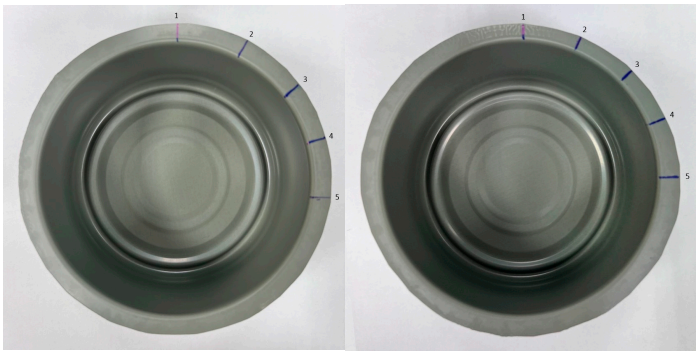

(**a**) (**b**)

Figure 20. Flange length measurement locations: (**a**) SULC; (**b**) Al-killed.

From 10 samples of each type of steel (Al-killed and SULC), the average flange length after re-drawing at five locations is presented in Figure 21. Al-killed steel exhibits more nonuniform flange lengths compared to SULC, with ranges of 1.24 mm for SULC and 1.76 mm for Al-killed. For distortion printing purposes, SULC is preferable.

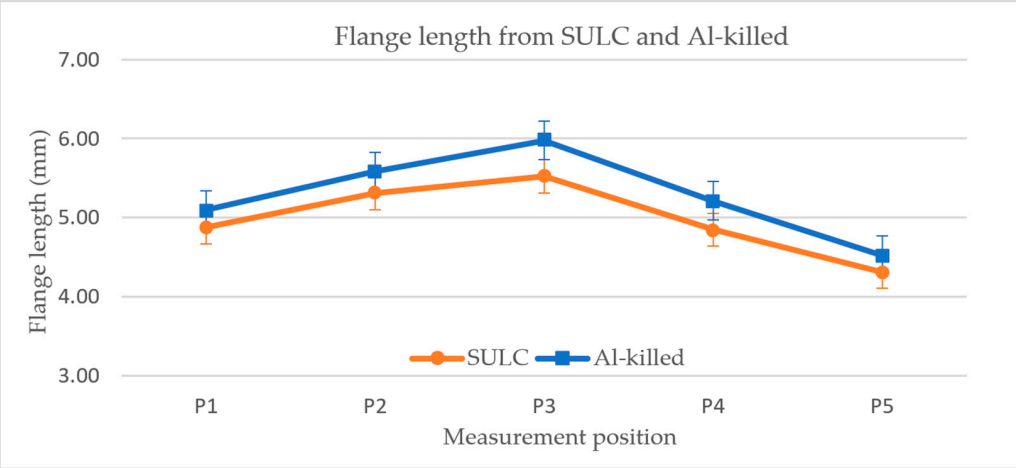

Figure 21. Averaged flange length from SULC and Al-killed.

To further investigate production variations, a larger sample size of 1800 samples is analyzed. These samples are categorized into four groups: G1 (poor, waving height > 2.0 mm), G2 (fair, waving height 1.1–2.0 mm), G3 (good, waving height 0.5–1.0 mm), and G4 (excellent, waving height < 0.5 mm). Experimental measurements are conducted using a microscope. The flange lengths obtained from each group are presented in Figure 22. The results indicate the following distribution: G1 (waving height > 2 mm: 0.4%), G2 (waving height 1.1–2.0 mm: 1.5%), G3 (waving height 0.5–1.0 mm: 55.56%), and G4 (waving height < 0.5 mm: 42.85%). G4 is selected to represent the standard case for further analysis.

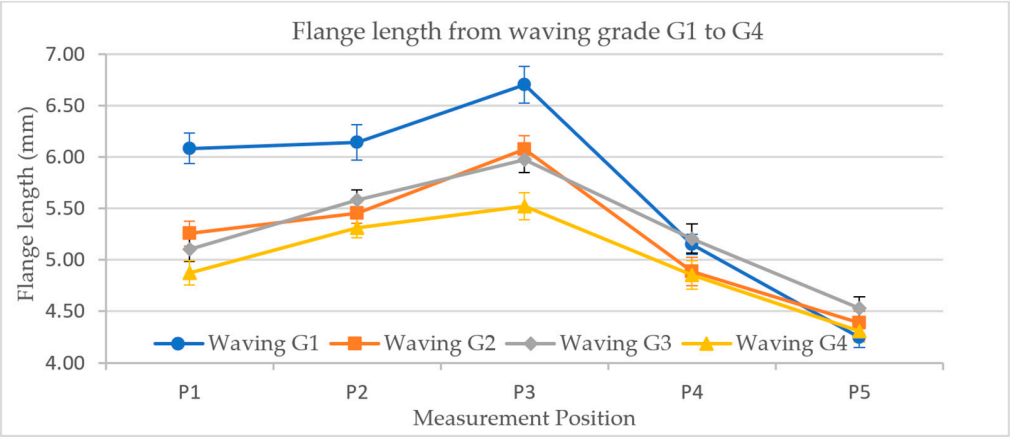

Figure 22. Comparison of flange length distribution between waving grade G1 to G4.

FEA results achieved with a die radius of 1.5 mm, COF of 0.03, $\overline{R}$ of 0.5, and ΔR value of −0.06 and 0.06 are compared with experimental results (waving G4) in Figure 23. The trend shows that ΔR at −0.06 gives a better agreement with the experiment in terms of the trend. Further parameter adjustments could improve the predictive accuracy.

FEA results achieved with a die radius of 1.5 mm, $\overline{R}$ of 0.5, ΔR of −0.06, BHF of 24,000 N, and COF of 0.03 and 0.06 are compared with experimental results (waving G4) in Figure 24. A higher value of COF results in a greater restraining force, leading to a greater flange length. However, the waving values remain largely unchanged (1.19 and 1.06 for COF of 0.03 and 0.06, respectively).

FEA results achieved with a die radius of 1.5 mm, $\overline{R}$ of 0.5, ΔR of −0.06, COF of 0.06, and BHF of 16,000 N and 24,000 N are compared with experimental results (waving G4) in Figure 25. A higher value of BHF results in a greater restraining force, leading to a greater

flange length. However, the waving values remain largely unchanged (1.09 and 1.06 for BHF = 16,000 and 24,000 N, respectively).

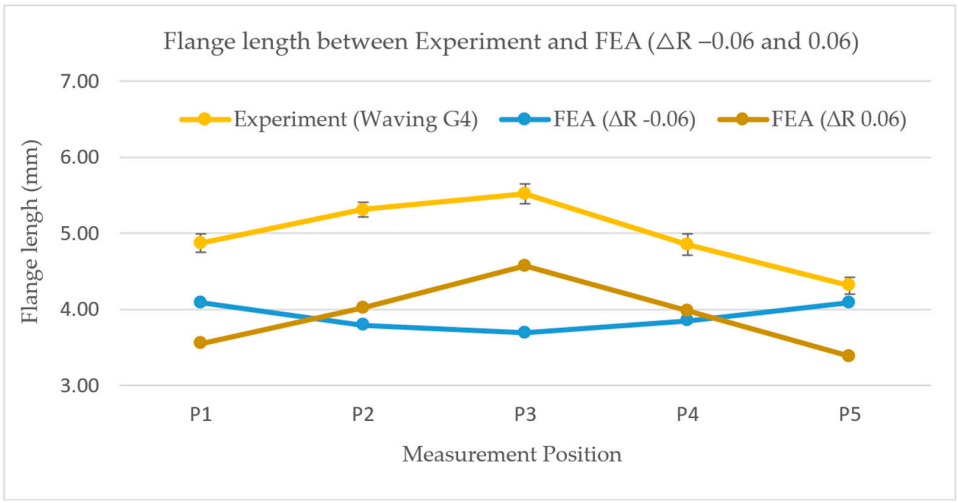

Figure 23. Flange length distribution from waving G4 and FEA (Difference of Δ*R*).

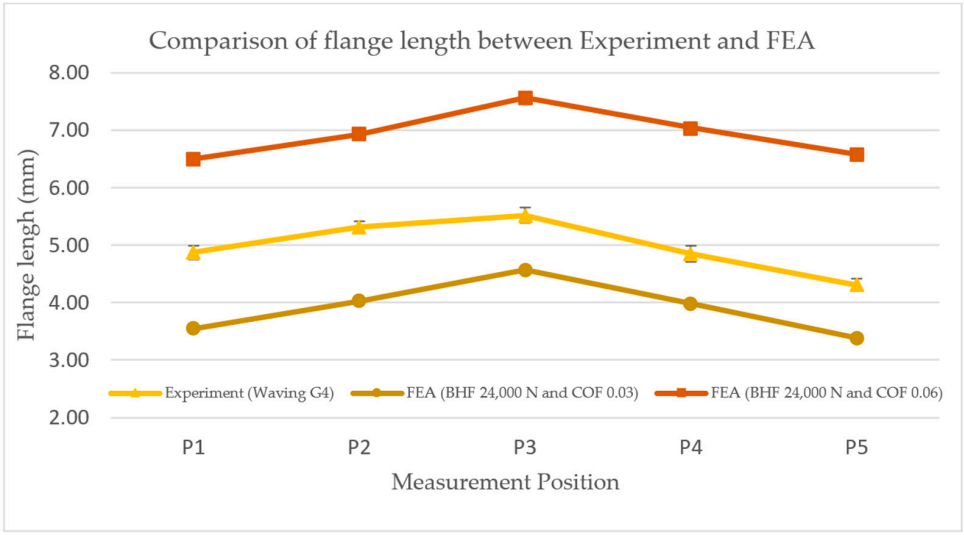

Figure 24. Flange length distribution from waving G4 and FEA (difference of COF).

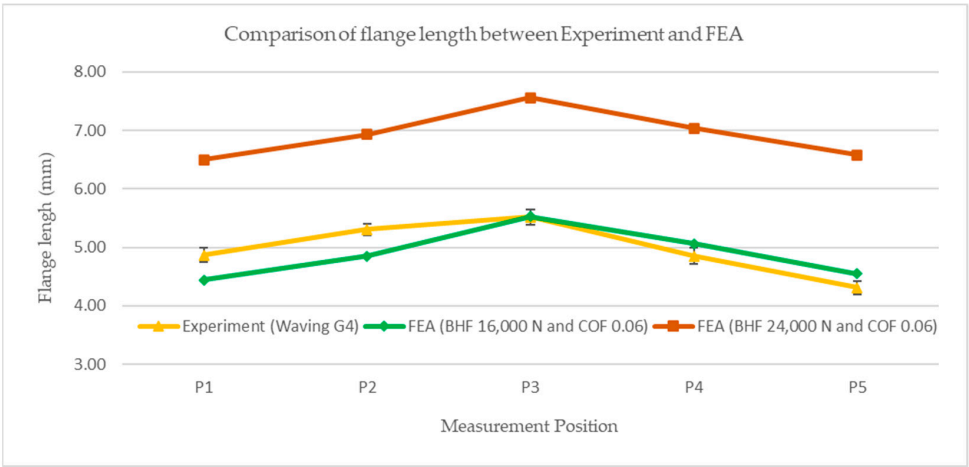

Figure 25. Flange length distribution from waving G4 and FEA (difference of BHF).

4. Scrap Rate Optimization

All production processes exhibit some degree of variation, which can lead to scrap or defects in a real DRD production. In can manufacturing systems, these uncertainties arise from various sources. Once these sources are identified and defined, the uncertainty of the forming process can be directly investigated using MCS. However, MCS is resource-intensive. To mitigate this, a metamodel can be employed to reduce the cost of MCS, allowing for the evaluation of the scrap rate. Additionally, process improvements are proposed to enhance the scrap rate. The workflow of this study is proposed and shown in Figure 26. The forming process, waving failure definition, distortion printing design, and material testing work together to create forming modeling. The model interacts with material parameter identification until the criteria are met. The waving evaluation is incorporated as part of the objective function. Variation is identified for uncertainty propagation, allowing the scrap rate to be evaluated and optimized.

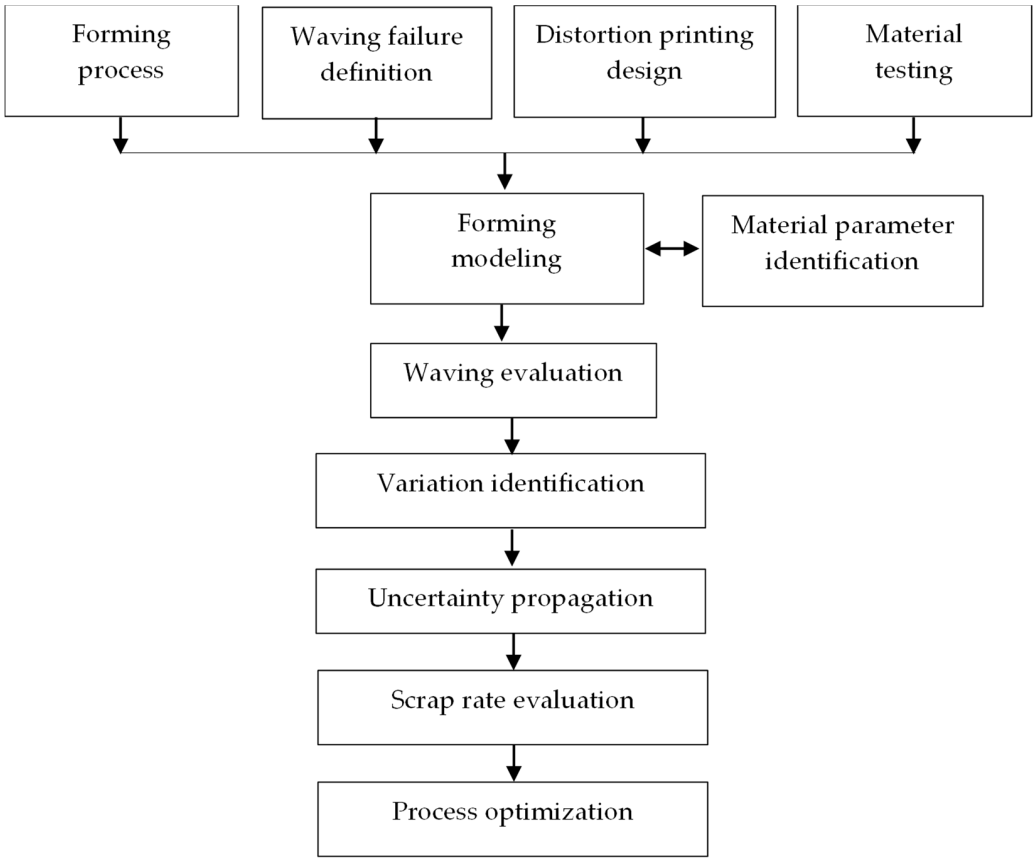

Figure 26. Workflow of the proposed method for scrap rate optimization.

4.1. Uncertainty Propagation via Metamodeling

The approach of uncertainty propagation begins with identifying parameters that exhibit variation. Assuming the tooling configuration is robust or somewhat rigid, this study focuses on five parameters: COF, $\overline{R}$, ΔR, δ, and BHF. The R values are defined as follows: $R45 = \overline{R} - \Delta R/2$, $R90 = \overline{R} + \delta$, and $R00 = 2\overline{R} + \delta - R90$. The waving value can be obtained through FEA. While MCS can directly investigate the uncertainty of the forming process, using FEA for uncertainty propagation is very resource-intensive and often impractical. Therefore, metamodeling with Latin hypercube sampling (LHS) is adopted to make MCS more practical.

LHS is a statistical method used to generate a near-random sample of parameter values from a multidimensional distribution. This sampling method is employed to construct computer experiments or for MCS, ensuring that much portion of the uncertain param-

eters are represented. LHS is utilized to create a sampling space for metamodeling. In MATLAB, LHS can be implemented using the command lhsdesign(n,p), which returns a Latin hypercube sample matrix of size n-by-p. In this work, n = 40, and p = 5. Once the range of each parameter is defined, the absolute value of each parameter can be obtained. FEA models are then created and evaluated according to the sample matrix. The results are applied to RBF to create a metamodel. The RBF implementation in MATLAB can be referenced from [24]. Uncertainty propagation is a method that transmits the uncertainties of independent variables through a model to estimate the uncertainty of the response. In this work, the response is the waving value.

The effect of uncertainty from the parameters of interest is investigated using MCS. In this study, MCS with 100,000 samples is conducted in MATLAB. These samples are analyzed to create the probability density function (PDF). The scrap rate (SR) is defined as the ratio of the number of prediction samples with a waving value greater than 1.0 mm. Five parameters are used to define variation in this study. Let $N(m,\sigma)$ represent a normal distribution with the mean (m) and the standard deviation (σ). The parameters under uncertainty are as follows: The friction coefficient (COF) is defined by $N(0.03, 0.003)$. $\overline{R}$ is defined by $N(0.5, 0.05)$. ΔR is defined by $N(-0.05, 0.006)$. δ is defined by $N(-0.02, 0.003)$. And the blank holder force (BHF) is defined by $N(20{,}000, 3000)$.

4.2. Process Improvement for Scrap Rate

The DRD process is executed using the relevant tooling discussed in Section 2.2. The punch is shaped according to the customer's specifications for the base of the part. The DRD process involves complex material flow and force distributions, with the key to successful operation being the ability to control the metal's flow. Several factors influence the extent of stretch and flow during the metal-forming process, including the mechanical properties of the metal, the geometry of the part being formed, friction, and processing conditions.

According to FEA results, a significant factor in the DRD process is the blank holder radius. It is proposed to explore the blank holder lip (adding radius to the blank holder), as shown in Figure 27. This exploration is expected to improve the material flow during the DRD process.

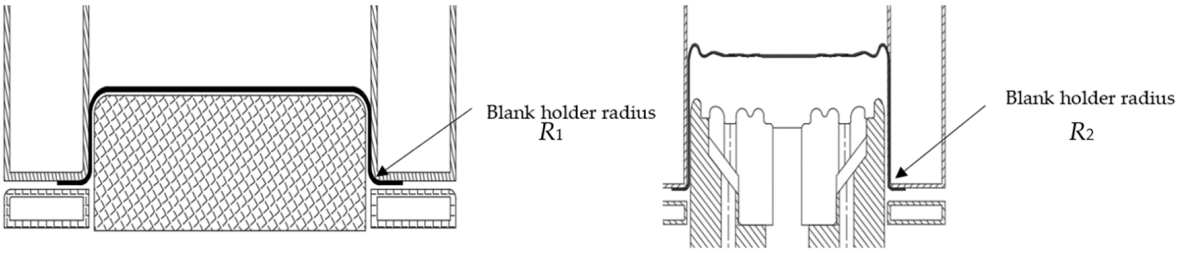

Figure 27. Tooling modification at blank holder radius: (**a**) drawing; (**b**) redrawing.

Four scenarios are explored. Each is defined by the blank holder radius at drawing and redrawing: (R_1, R_2). The scenarios are as follows: Case1 is (1.5, 1.5). Case2 is (2.0, 2.0). Case3 is (2.0, 1.5). And Case4 is (1.5, 2.0). The design space and waving values for four scenarios are presented in Table 3, with the last four columns indicating the corresponding waving values.

These scenarios are evaluated using the uncertainty propagation method described in the previous section. The results of interest, namely SR and PDF of the waving, are illustrated in Figure 28. The domain marked with a green arrow represents the accepted cans, while the domain marked with a red arrow represents the rejected cans. Uncertainty from these parameters affects SR. COF and BHF may vary due to process control, while the R-value, a material property, fluctuates during manufacturing. The R-value significantly impacts SR due to the nature of the waving. The shape of the PDF from these scenarios is

somewhat normally distributed, assuming the inputs follow a normal distribution. The behavior of the input parameter variations depends on real system observations and process control capabilities.

Table 3. The design space and corresponding waving value.

#	COF	BHF	*R*00	*R*45	*R*90	Case1	Case2	Case3	Case4
1	0.044	21,736	0.482	0.482	0.458	0.558	0.436	0.475	0.595
2	0.043	16,136	0.472	0.538	0.452	1.220	1.126	1.157	1.250
3	0.011	18,536	0.475	0.508	0.508	0.544	0.431	0.502	0.565
4	0.049	16,936	0.485	0.485	0.535	0.398	0.315	0.374	0.407
5	0.031	17,464	0.458	0.458	0.545	0.490	0.418	0.439	0.509
6	0.018	23,064	0.452	0.452	0.468	0.305	0.231	0.273	0.360
7	0.021	22,000	0.488	0.498	0.515	0.397	0.286	0.309	0.402
8	0.024	18,800	0.402	0.548	0.502	1.504	1.395	1.435	1.530
9	0.053	23,336	0.455	0.545	0.455	1.292	1.224	1.252	1.348
10	0.056	16,400	0.452	0.528	0.492	0.976	0.834	0.895	1.067
11	0.028	19,064	0.465	0.465	0.475	0.377	0.239	0.292	0.411
12	0.054	19,864	0.418	0.525	0.532	1.000	0.809	0.889	1.059
13	0.059	22,536	0.472	0.472	0.488	0.497	0.423	0.433	0.517
14	0.023	23,600	0.425	0.535	0.505	1.300	1.215	1.257	1.395
15	0.046	17,200	0.455	0.455	0.478	0.550	0.415	0.454	0.600
16	0.013	20,400	0.445	0.518	0.518	0.841	0.724	0.753	0.939
17	0.016	19,600	0.432	0.542	0.485	1.226	1.150	1.211	1.329
18	0.041	21,464	0.415	0.532	0.522	1.063	0.955	0.994	1.116
19	0.038	22,264	0.488	0.488	0.525	0.370	0.312	0.343	0.397
20	0.058	22,800	0.462	0.505	0.528	0.710	0.650	0.665	0.745
21	0.029	18,264	0.472	0.515	0.498	0.685	0.573	0.592	0.724
22	0.014	21,200	0.468	0.468	0.465	0.340	0.281	0.338	0.381
23	0.048	20,936	0.492	0.492	0.482	0.539	0.421	0.455	0.557
24	0.051	18,000	0.468	0.495	0.542	0.530	0.433	0.475	0.566
25	0.039	16,664	0.462	0.462	0.472	0.422	0.321	0.340	0.465
26	0.033	20,664	0.418	0.522	0.538	1.011	0.825	0.851	1.023
27	0.036	23,864	0.475	0.475	0.512	0.421	0.352	0.392	0.425
28	0.026	19,336	0.478	0.478	0.548	0.424	0.354	0.387	0.427
29	0.034	20,136	0.512	0.512	0.462	0.580	0.524	0.552	0.600
30	0.019	17,736	0.502	0.502	0.495	0.386	0.307	0.325	0.397
31	0.046	18,904	0.511	0.514	0.461	0.698	0.609	0.656	0.752
32	0.036	17,104	0.456	0.456	0.529	0.392	0.365	0.379	0.412
33	0.057	22,104	0.491	0.511	0.486	0.657	0.582	0.611	0.711
34	0.054	21,904	0.499	0.499	0.476	0.582	0.552	0.569	0.684
35	0.023	23,504	0.486	0.489	0.536	0.330	0.297	0.314	0.340
36	0.029	21,104	0.406	0.531	0.531	1.150	1.066	1.080	1.208
37	0.031	22,704	0.446	0.526	0.501	0.970	0.836	0.850	1.010
38	0.037	17,504	0.479	0.479	0.479	0.477	0.298	0.347	0.492
39	0.019	21,304	0.401	0.529	0.541	1.244	1.128	1.174	1.311
40	0.041	16,704	0.496	0.496	0.491	0.481	0.354	0.411	0.512

The predicted SR of 7.9% in Case1 is similar to the 8.3% obtained in the original case without the compensation and rotation techniques presented in Section 2.1. Case2 offers the best scrap rate value, with an estimated SR of 1.6%, although this is still higher than the industry-desirable rate of 0.25%. In real production, techniques such as rotation and compensation, mentioned in Section 2.1, are useful for reducing graphical distortion. By analogy, similar improvements could reduce the predicted SR from 1.6% to an even lower value. However, this study focuses on material flow during the forming process, and such graphical techniques do not impact this evaluation. Additionally, Case3 may be preferable for industry since the final part shape remains unchanged.

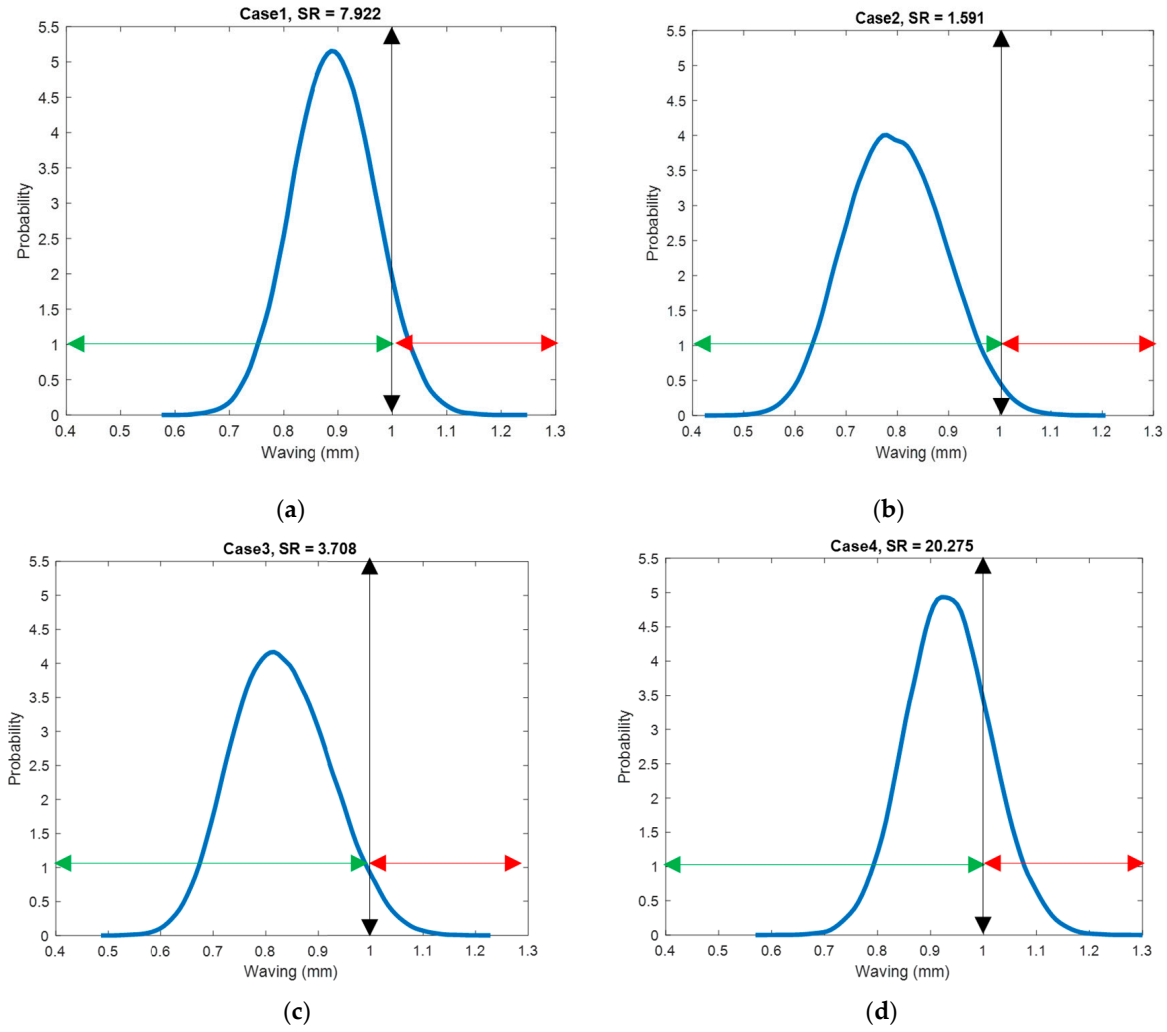

Figure 28. Scrap rate: (**a**) Case1; (**b**) Case2; (**c**) Case3; (**d**) Case4.

Figure 29 presents an FEA prediction based on the nominal values after drawing in Case1 and Case2. The improved thinning distribution, observed through reduced deformation and less thinning at the sidewall, indicates a positive impact. Figure 30 presents an FEA prediction based on the nominal values after redrawing in Case1 and Case2. The improved thinning distribution, observed through reduced deformation and less thinning, indicates a positive impact. Future work could explore and implement further improvements to enhance SR.

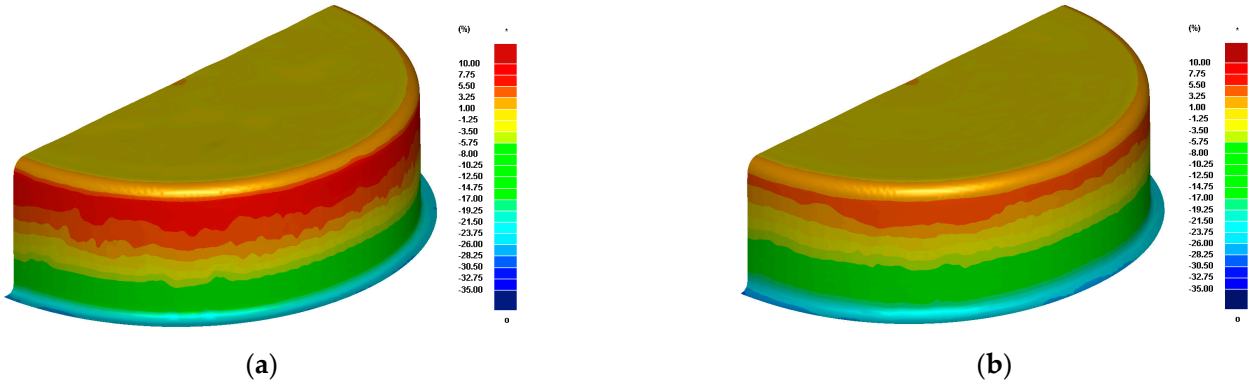

Figure 29. Nominal thinning prediction after drawing: (**a**) before modification; (**b**) after modification.

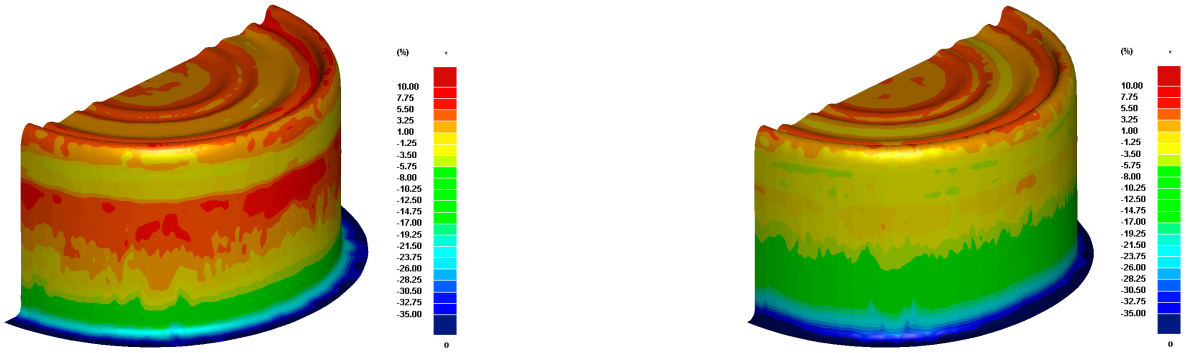

(**a**) (**b**)

Figure 30. Nominal thinning prediction after redrawing: (**a**) before modification; (**b**) after modification.

5. Conclusions

The industrial production of food cans has evolved from traditional labeling to premium cans with distortion printing, which have different quality requirements. In addition to traditional formability, waving is now a critical quality requirement for premium can production. To save materials, modern food cans use stronger materials and a thinner sheet. This study utilizes a DR low-carbon steel sheet and chromium-coated TFS with a thickness of 0.16 mm. An FEA model is developed to simulate the forming process. A material parameter identification method is proposed and illustrated, achieving a good agreement with real-world data. In response to real manufacturing processes, the scrap rate is the key performance index. This work presents an uncertainty propagation method to estimate the scrap rate in premium food can forming under waving requirements, addressing both uncertain parameters and a large number of design variables. RBF neural network is essential for reducing the computational burden during uncertainty propagation via MCS. Scrap rate optimization is conducted, and several possible scenarios are proposed and evaluated using the uncertainty propagation method. The predicted results in the base case show a good agreement with observations from real production. Recommendations to improve the scrap rate are also proposed.

Author Contributions: Conceptualization, N.C. and P.T.; methodology, N.C. and P.T.; validation, N.C.; formal analysis, N.C. and P.T.; investigation, N.C. and P.T.; resources, N.C. and P.T.; data curation, N.C.; writing—original draft preparation, N.C. and P.T.; writing—review and editing, N.C. and P.T.; visualization, N.C. and P.T.; supervision, P.T.; project administration, P.T.; funding acquisition, P.T. All authors have read and agreed to the published version of the manuscript.

Funding: The research leading to these results received funding from King Mongkut's University of Technology Thonburi (KMUTT), Thailand Science Research and Innovation (TSRI), and National Science, Research, and Innovation Fund (NSRF) under Fundamental Fund 2022.

Institutional Review Board Statement: Not applicable.

Informed Consent Statement: Not applicable.

Data Availability Statement: The original contributions presented in the study are included in the article, and further inquiries can be directed to the corresponding author.

Conflicts of Interest: The authors declare no conflicts of interest.

References

1. Boz, Z.; Sand, C.K. A Systematic Analysis of the Overall Nutritional Contribution of Food Loss and Waste in Tomatoes, Spinach, and Kidney Beans as a Function of Processing. *J. Food Process Eng.* **2020**, *43*, 11–12. [CrossRef]
2. Andress, E.L.; Harrison, J.A. *So Easy to Preserve*, 5th ed.; Cooperative Extension Service, The University of Georgia: Athens, GA, USA, 2006.

3. Yoichiro, Y.; Hiroki, I.; Toyofumi, W. Development of Laminated Tin Free Steel (TFS) "UNIVERSAL BRITE®" Type F for Food Cans. *JFE Technol. Rep.* **2007**, *9*, 49–53. Available online: https://www.jfe-steel.co.jp/en/research/report/009/pdf/009-11.pdf (accessed on 30 June 2021).
4. Singh, S.; Agrawal, A.; Sharma, D.; Saini, V.; Kumar, A.; Praveenkumar, S. Implementation of Total Productive Maintenance Approach: Improving Overall Equipment Efficiency of a Metal Industry. *Inventions* **2022**, *7*, 119. [CrossRef]
5. Browne, M.T.; Hillery, M.T. Optimising the variables when deep-drawing C.R.1 cups. *J. Mater. Process Technol.* **2003**, *136*, 64–71. [CrossRef]
6. Antonio, C.A.C.; Dourado, N.M. Metal-forming Process Optimisation by Inverse Evolutionary Search. *J. Master Process Technol.* **2002**, *121*, 403–413. [CrossRef]
7. Wei, D.L.; Cui, Z.S.; Chen, J. Optimization and Tolerance Prediction of Sheet Metal Forming Process Using Response Surface Model. *Comput. Mater. Sci.* **2008**, *42*, 228–233. [CrossRef]
8. Barros, P.D.; Alves, J.L.; Oliveira, M.C.; Menezes, L.F. Study on the effect of tension-compression asymmetry on the cylindrical cup forming of an AA2090-T3 alloy. *Int. J. Solids Struct.* **2018**, *151*, 135–144. [CrossRef]
9. Coppieters, S.; Traphoner, H.; Stiebert, F.; Balan, T.; Kuwabara, T.; Tekkaya, A.E. Large Strain Flow Curve Identification for Sheet Metal. *J. Mater. Process. Technol.* **2022**, *308*, 117725. [CrossRef]
10. Jiaa, Q.; Song, X.; Jic, M.; Chaia, H.; Lua, S. Isogeometric Algorithm for One-Step Inverse Forming of Sheet Metal. *Comput. Methods Appl. Mech. Engrg* **2023**, *404*, 115778. [CrossRef]
11. Kleiber, M.; Knabel, J.; Rojek, J. Response Surface Method for Probabilistic Assessment Metal Forming Failures. *Int. J. Numer. Methods Eng.* **2004**, *60*, 51–67. [CrossRef]
12. Jansson, T.; Nilsson, L.; Moshfegh, R. Reliability Analysis of a Sheet Metal Forming Process Using Monte Carlo Analysis and Metamodels. *J. Mater. Process Technol.* **2008**, *202*, 255–268. [CrossRef]
13. Ou, H.; Wang, P.; Lu, B.; Long, H. Finite element modelling and optimisation of net-shape metal forming processes with uncertainties. *Comput. Struct.* **2012**, *90–91*, 13–27. [CrossRef]
14. Arnst, M.; Ponthot, J.P.; Boman, R. Comparison of stochastic and interval methods for uncertainty quantification of metal forming processes. *Comptes Rendus Mécanique* **2018**, *346*, 634–646. [CrossRef]
15. Huang, C.; Radi, B.; Hami, A.E. Uncertainty analysis of deep drawing using surrogate model based probabilistic method. *Int. J. Adv. Manuf. Technol.* **2016**, *86*, 3229–3240. [CrossRef]
16. Polini, W.; Corrado, A. Uncertainty in Manufacturing of Lightweight Products in Composite Laminate: Part 1—Numerical Approach. *Int. J. Adv. Manuf. Technol.* **2019**, *101*, 1423–1434. [CrossRef]
17. Marques, A.E.; Prates, P.A.; Pereira, A.F.G.; Oliveira, M.C.; Fernandes, J.V.; Ribeiro, B.M. Performance Comparison of Parametric and Non-Parametric Regression Models for Uncertainty Analysis of Sheet Metal Forming Processes. *Metals* **2020**, *10*, 457. [CrossRef]
18. Galetto, M.; Verna, E.; Genta, G.; Franceschini, F. Uncertainty evaluation in the prediction of defects and costs for quality inspection planning in low-volume productions. *Int. J. Adv. Manuf. Technol.* **2020**, *108*, 3793–3805. [CrossRef]
19. Silva, A.F.; Marins, F.A.S.; Oliveira, J.B.S.; Dias, E.X. Multi-objective optimization and finite element method combined with optimization via Monte Carlo simulation in a stamping process under uncertainty. *Int. J. Adv. Manuf. Technol.* **2021**, *117*, 305–327. [CrossRef]
20. Trzepieciński, T.; Szwajka, K.; Szewczyk, M. An Investigation into the Friction of Cold-Rolled Low-Carbon DC06 Steel Sheets in Sheet Metal Forming Using Radial Basis Function Neural Networks. *Appl. Sci.* **2023**, *13*, 9572. [CrossRef]
21. Penalva, M.; Martín, A.; Ruiz, C.; Martínez, V.; Veiga, F.; Val, A.G.d.; Ballesteros, T. Application-Oriented Data Analytics in Large-Scale Metal Sheet Bending. *Appl. Sci.* **2023**, *13*, 13187. [CrossRef]
22. Tricarico, L.; Palmieri, M.E. Robust Design of Deep Drawing Process through In-Line Feedback Control of the Draw-In. Appl. *Sci.* **2023**, *13*, 1717. [CrossRef]
23. Chang, D.F.; Wang, J.E. Analysis of Draw-redraw Processes. *Int. J. Mech. Sci.* **1998**, *40*, 793–804. [CrossRef]
24. Chirokov, A. Scattered Data Interpolation and Approximation Using Radial Base Functions. MATLAB Central File Exchange. 2022. Available online: https://www.mathworks.com/matlabcentral/fileexchange/10056-scattered-data-interpolation-and-approximation-using-radial-base-functions (accessed on 28 March 2022).